



3RD YEAR INDEPENDENT RESEARCH ESSAY

**Towards quantum computation based on optically
interfaced NV centre spins**

by:

Kutloano Lephoto Nkojoana

Advanced Experimental Physics III

of the

School of Physics,
Faculty of Science,
University of the Witwatersrand

October 5, 2024

Abstract

This paper investigates the potential of nitrogen-vacancy (NV) centers in diamond as a platform for quantum computing. NV centers exhibit unique electronic and spin properties, making them prime candidates for use in quantum registers and single-photon sources. The paper explores the electronic structure, photophysical characteristics, and spin properties of NV centers, emphasizing their manipulation through hyperfine interactions and microwave pulses. Additionally, it reviews the dynamics of quantum gates and the potential for two-qubit operations using electron-nuclear spin systems. This review provides insight into the experimental setup, challenges, and prospects of integrating NV centers into scalable quantum networks.

Literature Review

The exploration of nitrogen-vacancy (NV) centers as candidates for quantum computing has garnered significant attention in recent decades. Early foundational work by Jelezko and Wrachtrup laid the groundwork for understanding NV centers as quantum registers, providing insights into their spin properties and demonstrating optical initialization and readout of single spins. This work was critical in establishing NV centers as practical qubits due to their long coherence times, even at room temperature.

Further theoretical and experimental research has advanced the understanding of NV centers' electronic structure and photophysical properties. Doherty et al. (2013) offered a comprehensive review of the NV center's electronic configuration, focusing on the interactions between electron spins and the surrounding diamond lattice. Their *ab initio* calculations demonstrated how the spin properties of NV centers could be manipulated for quantum information processing. Gali and colleagues expanded on this by conducting advanced density functional theory (DFT) calculations, providing insights into the energy levels and hyperfine interactions that form the basis for qubit operations.

The use of NV centers in two-qubit quantum gates has been a subject of intense research. Neumann et al. (2010) demonstrated how coupled electron and nuclear spins could be used to create quantum registers, emphasizing the role of hyperfine interactions for achieving coherence and control over nuclear spins. This work paved the way for more sophisticated quantum gate operations involving both electron and nuclear spins, as demonstrated by Bradley et al. (2019), who achieved a 10-qubit solid-state spin register, significantly advancing the scalability of NV center-based quantum systems.

Optically interfaced NV centers have been further explored for their potential as single-photon sources in quantum communication and optical quantum computing. Awschalom, Hanson, and colleagues (2018) provided an in-depth discussion of using NV centers in diamond for spintronics and quantum sensing, emphasizing their utility as stable sources of single photons at room temperature. However, as Kurtsiefer et al. (2000) showed, NV centers are not without limitations, particularly in their broad emission spectrum, which reduces their efficiency compared to other defects like silicon-vacancy (SiV) centers.

The development of quantum logic gates using NV centers has been a major focus in recent years. Rong et al. (2015) successfully demonstrated fault-tolerant universal quantum gates under ambient conditions, making significant progress toward practical quantum computers. Their work, combined with Fox's (2006) introduction to quantum optics, laid the foundation for understanding the optical manipulation of NV centers for quantum information processing.

Finally, the challenges of scaling NV center-based quantum systems have been extensively addressed in the literature. Maze et al. (2011) and Taminiau et al. (2019) discussed the impact of decoherence and the strategies for error correction and mitigation in NV center qubits, particularly in the presence of spin-orbit coupling and magnetic noise. These studies underline the importance of addressing environmental factors to improve the performance of NV-based quantum networks.

Introduction

The appeal of quantum computers arises from the advantages they promise to offer over classical computers [1]. They are suggested to offer exponentially faster operations for particular tasks such as searching databases, fourier transformations, factorising large integers and simulating important quantum systems [1]. To realize a quantum computer, scalable physical qubits which can be initialized, measured and interacted with to develop quantum logic gates are required[1].

It is generally accepted that solid structures will be the main vehicle for increasing the number of qubits to the practically useful number (roughly several hundreds). Moreover, isolated electron and nuclear spins in solids are considered to be among the most promising candidates for implementing qubits for quantum processors [2]-[3]. These spins are particularly robust to changes in temperature, opening the possibility for quantum computing operations at room temperature [4]. However, spins in solid materials often suffer from two problems, namely spin-orbit coupling and quantum decoherence due to magnetic noise, however, in diamond, both these effects are very weak [5].

Diamond with low spin-orbit coupling and a spin-free lattice, supports a variety of impurities and defects that give rise to optical bands at energies throughout the infrared and visible spectrum[3]. There are defects in diamond with unique spectral signatures, these optically active sites can give an otherwise transparent diamond a tinted appearance. These point defects include the nitrogen-vacancy(NV) centre, silicon-vacancy centre, the tin-vacancy centre, the germanium vacancy centre as well as other variants which have been uncovered and analysed over the past two decades.[6]. This article will focus solely on the NV centre defect.

The NV centre is an atomic point defect with C_{3v} symmetry consisting of a nitrogen impurity atom as well as an adjacent carbon vacancy oriented along the $\langle 111 \rangle$ crystalline direction[7]. A model of the defect structure is in Fig.1. There are two main fabrication techniques for NV centres in diamond, namely electron irradiation and annealing as well as nitrogen ion implantation [8]. The first technique is performed on diamond substrates that already contain nitrogen, specifically type 1b diamond formed through high-pressure and

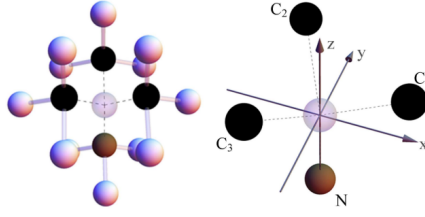


Figure 1: Schematic diagram of the symmetry of the the defect centre to the left and diagram indicating the coordinate system for the centre to right, the $\langle 111 \rangle$ direction is along the z-axis. The vacancy(transparent) is at the centre(transparent), the adjacent nitrogen atom(brown) near the bottom, the closet carbon atoms(black) near the vacancy, neighbouring carbon atoms(white) are further away from the vacancy.

high temperature(HBHT) [9]. Through this method, electron bombardment leads to radiation damage within the crystal and introduces vacancies, further annealing treatments(at $T > 825K$) to the crystals enable the vacancies to migrate towards the nitrogen spots and form NV defects [8]. Ion implantation followed by high temperature ($T > 1100K$) annealing is the most efficient and straightforward method to fabricate localized NV centres in a controlled manner [8]. Here N^+ ions are implanted, creating vacancies and adding interstitial defects [10]. Multiple annealing steps follow which combine the nitrogen defects with the vacancies and form the NV centres [10]. A more pure (near defect free) substrate which can be produced through microwave plasma-assisted chemical vapour deposition(MPCVD) is required for the ion implantation procedure [10].

The defect centre has four known charge states: NV^- , NV^{-2} , NV^0 and NV^+ [6]. The negatively charged NV centre in diamond is formed by trapping six electrons in localized atomic-like orbitals, shielded from charge scattering due to the wide band band gap of diamond[11]. Two of the six electrons are unpaired and combine to form a triplet ground and excited state[12]. This gives rise to a more intricate energy structure which makes it the most suitable among the four for application in quantum information processing(QIP) [5]. Therefore, the scope of this review is limited to the negatively charged NV centre NV^- and will be referred to as just the NV centre from here on. Single NV centres can be imaged using scanning confocal microscope [13] as shown in Fig. 2. The NV centre combines a long-lived electronic spin ($S=1$) with a robust optical interface, allowing for optical imaging as well as high fidelity initialisation, manipulation and readout of the spin states [11]. An antibunching signature has been observed from single NV centre emissions, making the NV centre a possible candidate for on-demand single photon generation [4]. This as well as the photostability of diamond defects are important for the realisation of optical quantum information processing schemes [4].

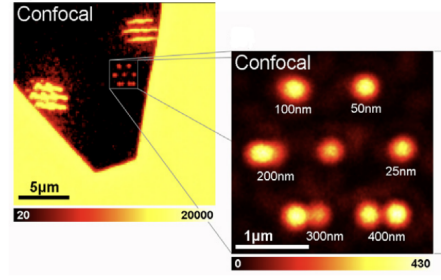


Figure 2: Scanning confocal microscope image showing fluorescence from optically active single NV centres.

The NV centre is suggested to be an attractive candidate as a platform for a quantum register. Quantum registers are quantum mechanical systems consisting of qubits that can be coherently controlled for scalable quantum information processing, such as quantum communication and distributed quantum computation[14]-[15]. The basis for an NV centre quantum register are quantum logic gates schemes using the electronic and nuclear spins contained in an NV centre in diamond [16]. The electron spins provide an efficient control and high fidelity readout protocol that can be extended to coherently control nuclear spins via hyperfine interactions[15]. The nuclear spins supply long lasting qubits which can be used to store and process quantum states [16]. In this review the mechanism behind single-qubits as well as electron-nuclear two-qubit gates will be discussed. Specifically, a conditional rotation(CROT) logic gate, whose physical carriers were single electron and nuclear spins of the $NV + ^{13}C$ centre are explored.

In the following chapters the quantum properties of the defect centre will be discussed, following it's potential role in linear quantum computing as a single photon source will be addressed. Lastly a detail of how it could serve a role as the platform for a quantum register is given in the final section.

Chapter 1

Quantum Properties of NV Centres

1.1 Electronic structure of the NV Centre

The structure of the NV defect, accompanied with the defined C_{3v} symmetry axis $\langle 111 \rangle$ ¹ is shown in Fig. 1.1 [15].

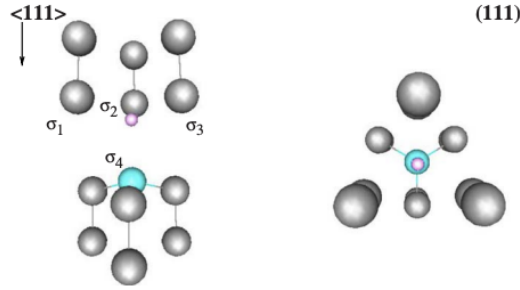


Figure 1.1: The NV centre viewed from the side(left) and along the $\langle 111 \rangle$ direction. The carbon vacancy site is represented by a pink circle and the nearest neighbour carbon and nitrogen atoms by grey and cyan balls, respectively

Experiments show that six electrons are localized at the vacancy site for the negatively charged NV centre [15]. This vacancy leads to unsatisfied bonds originating from three adjacent carbon atoms as well as the substitutional nitrogen atom.[15]. The unsatisfied bonds correspond to four hybridized orbitals sp^3 which are referred to as "dangling bonds" labeled σ_i (for $i = 1, 4$), which point inward on the vacancy [15]. Due to the localization of the unpaired electrons at the vacancy, the dangling bonds σ_{1-4} can be used to model

¹passing through the nitrogen atom and the vacancy site

single-electron orbitals around the defect[17]. The single-electron orbitals are approximated through molecular orbital theory, configuring the dangling bonds into linear combinations of atomic orbitals(LCAOs)² [18]. The exact combinations that construct the single-electron orbitals φ_r are determined by the crystal field of the defect and can be calculated by transforming the dangling bonds under the irreducible representation(IR) of the point group of the defect. [17],

$$\varphi_r = P^{(r)}\sigma_i = \frac{l_r}{h} \sum_e \chi_e^{(r)} R_e \sigma_i \quad (1.1.1)$$

where $P^{(r)}$ is the projection operator to the IR r , $\chi^{(r)}_e$ is the character of operation the element R_e for the IR r , l_r is the dimension of the IR r , and h gives the number of elements of the group. The following orthonormal states form after operation of the eq. 1.1.1 onto the dangling bonds σ_{1-4} :

$$a_1(1) = \sigma_4, a_1(2) = \frac{1}{\sqrt{3}\sqrt{1+2S_{cc}-3S_{nc}^2}}(\sigma_1 + \sigma_2 + \sigma_3 - 3S_{nc}\sigma_4)$$

$$e_x = \frac{1}{\sqrt{3}\sqrt{2-2S_{cc}}}(2\sigma_1 - \sigma_2 - \sigma_3), e_y = \frac{1}{\sqrt{2-2S_{cc}}}(\sigma_2 - \sigma_3)$$

where $S_{nc} = \langle \sigma_4 | \sigma_1 \rangle$ and $S_{cc} = \langle \sigma_1 | \sigma_2 \rangle$ are orbital overlap integrals.

Ab initio studies show that the $a_1(1)$ and $a_1(2)$ single-electron orbitals have mixed to form $a'_1(1)$ such that $a'_1(1)$ has low energy and falls into the diamond valence band [18]. Ab initio density functional theory (DFT) calculations revealed that the $a_1(1)$ and $a_1(2)$ levels are lower than the e_x and e_y levels [17]. The calculated single-electron levels with respect to the valence band of bulk diamond are shown in Fig. 1.2 for the ground state of the NV centre [19]. There are six single-electron orbitals corresponding to spin-up and spin-down present in the band gap with (a_1, e_x, e_x) symmetry occupied by four electrons [20]-[19]. The spin-up and spin-down of the a_1 orbitals are fully occupied, however, only the spin-up orbitals of e symmetry are filled while their spin-down orbitals are unoccupied[19]. The other two of the six electrons associated with the centre occupy the a'_1 orbitals within the diamond valence band and do not influence the observable properties of the centre [20]. The NV centre is referred to as a deep-level defect due to the discrete energy levels that lie within the diamond bandgap[7].

²While the employment of this method could be considered to be an over approximation, neglecting interactions between the vacancy single-electron orbitals and the electron orbitals dormant in the remainder of the crystal, the purpose of this method is only to predict the correct number of single-electron orbitals that correspond to a symmetry group and to approximate the energy level order of the defect orbitals [18].

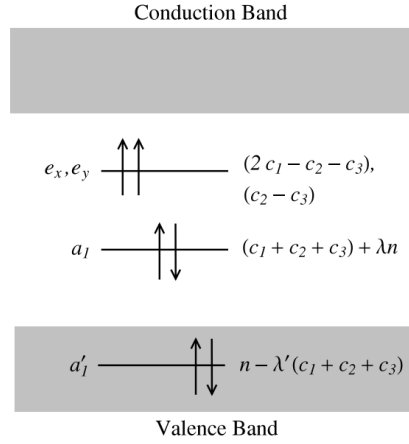


Figure 1.2: Visualization of the many-electron ground state of the NV centre with 3A_2 representation, where six electrons populate the calculated single-electron spin-resolved orbitals. Two electrons occupy the spin-up and spin-down levels down in the valence band (this state is neglected in the review), the next two electrons occupy the a_1 symmetry states and the two remaining electrons populate two degenerate orbitals of e symmetry (e_x and e_y).

The configuration of two electrons situated into the four possible quantum states corresponding to e_x and e_y (configuration denoted as e^2), results in the following possible many-electron states: 3A_2 , 1A_1 and 1E . Experiments have indicated 3A_2 to be the ground state of the defect [15]. If one electron is excited from $a_1(2)$ into the e level (e_x or e_y) then a state 3E or 1E with configuration $a_1^1(2)e^3$ is obtained [15]. In situations where both electrons are excited from $a_1(2)$ to the e_x and e_y orbitals then a fully symmetric 1A_1 state with configuration $a_1^0(2)e^4$ is obtained [15]. Since the spin state cannot be changed during excitation and emission, it is found that ${}^3A_2 \rightarrow {}^3E$ is the only allowed transition to first order [15] and only this transition contributes to the fluorescence of the NV centre [4]. These electron configurations give rise to a triplet ground state with an optically active $S=1$ excited state with below bandgap (5.4 eV) excitation energy and two metastable singlet states 1E and 1A_1 [21]. The wavefunctions of the triplet and singlet states are compiled in Fig. 1.3.

Configuration	Γ	M_S	(x,y)	Wave function
$a_1^2(2)e^2$	3A_2	1		$ 2\bar{2}34\rangle$
		0		$\frac{1}{\sqrt{2}}[2\bar{2}3\bar{4}\rangle + 2\bar{2}\bar{3}4\rangle]$
		-1		$ 2\bar{2}\bar{3}\bar{4}\rangle$
	1A_1	0		$\frac{1}{\sqrt{2}}[2\bar{2}3\bar{3}\rangle + 2\bar{2}4\bar{4}\rangle]$
		0	x	$\frac{1}{\sqrt{2}}[2\bar{2}3\bar{3}\rangle - 2\bar{2}4\bar{4}\rangle]$
	1E	0	y	$\frac{1}{\sqrt{2}}[2\bar{2}3\bar{4}\rangle - 2\bar{2}\bar{3}4\rangle]$
$a_1^1(2)e^3$	3E	1	x	$ 234\bar{4}\rangle$
			y	$ 23\bar{3}4\rangle$
		0	x	$\frac{1}{\sqrt{2}}[\bar{2}34\bar{4}\rangle + \bar{2}3\bar{4}4\rangle]$
			y	$\frac{1}{\sqrt{2}}[\bar{2}3\bar{3}4\rangle + 23\bar{3}\bar{4}\rangle]$
	1E	-1	x	$ \bar{2}34\bar{4}\rangle$
			y	$ \bar{2}3\bar{3}\bar{4}\rangle$
		0	x	$\frac{1}{\sqrt{2}}[\bar{2}34\bar{4}\rangle - \bar{2}3\bar{4}4\rangle]$
			y	$\frac{1}{\sqrt{2}}[\bar{2}3\bar{3}4\rangle - 23\bar{3}\bar{4}\rangle]$
$a_1^0(2)e^4$	1A_1	0		$ 3\bar{3}4\bar{4}\rangle$

Figure 1.3: The electronic configurations and the possible total wave functions with C_{3v} symmetry. Here the single-electron orbitals are abbreviated as numbers e.g $a_1(2) \rightarrow 2$ and thw overbar corresponds to the spin-down orbitals. The symmetry of the total wavefunction(Γ) and it's spin projection(m_S) are given in the second and third column respectively. For the doubly degenerate E state, the x and y transformations are assigned in the second last coloumn.

The spin projections for the triplet state are : $|m_S = 0\rangle$, $|m_S = -1\rangle$, $|m_S = +1\rangle$ and these 3 spin states are initially degenerate and thus occupy the same energy level [7]. The Hamiltonian including the energy V of each state 3A_2 , 3E 1A_1 ³ the spin-orbit V_{SO} and spin-spin V_{SS} interaction is given by:

$$H = V + V_{SO} + V_{SS} \quad (1.1.2)$$

where

$$V_{SO} = \lambda(L_z S_z) + \lambda'(L_x S_x - L_y S_y)$$

$$V_{SS} = \rho S_z^2 + \rho'(S_x^2 + S_y^2)$$

³There was not much information on the 1E state until recently so it is sometimes omitted in calculations and energy level diagrams

where λ , λ' , ρ and ρ' are the coefficients associated with the axial and non-axial interactions[22]. The spin-spin interactions between the unpaired electrons on the e level cause a splitting of the ground state into a singlet state $|A_2, S_z\rangle$ corresponding to $m_S = 0$, with symmetry A_1 and doublet $|A_2, S_x\rangle$ and $|A_2, S_y\rangle$ corresponding to $m_S = \pm 1$ with symmetry E [22]. The axial $\lambda(L_z S_z)$ spin-orbit interaction lifts the degeneracy of the excited spin triplet, splitting 3E into three two-fold degenerate states; E , E' , and an (A_1, A_2) pair [22]-[23]. The aspects of the NV centre's energy levels are represented in in Fig. 1.4.

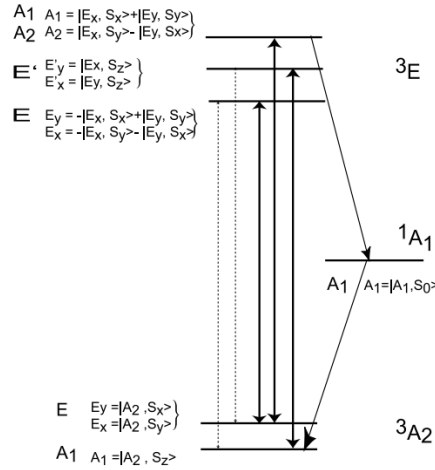


Figure 1.4: The zero-field energy levels of the N-V centre in C_{3v} symmetry. The single zero-field splitting between the $m_S = 0$ and $m_S = \pm 1$ spin sub-levels has been observed to have a magnitude of $D \sim 2.87$ GHz where D is the fine structure tensor [20]. Optically allowed transitions are indicated with solid arrows and the diagonal arrows display inter-system crossing enabled by spin-orbit interactions.

1.2 Photophysics of the NV Centre

1.2.1 Optical transitions

As discussed earlier, the transition ${}^3A_2 \leftrightarrow {}^3E$ is the only transition that can be detected through fluorescence, however, this is not the only transition that occurs upon optical excitation [4]. There are intersystem crossing (ISC) processes between the excited state 3E and ground state 3A_2 and the intermediate state 1A_1 . These ISC processes are induced by phonons and the parallel and perpendicular components of spin-orbit interaction [21].

We establish a basis T_i with $i = X, Y, Z$ where X , Y and Z correspond to the spin projections $m_S = 1$, $m_S = -1$ and $m_S = 0$ respectively. The ground and excited state spin

sublevels are represented by T_{0i} and T_{1i} respectively. The rates of the transition from an excited state spin sublevel T_{1i} to the metastable state 1A_1 k_{TS} are different for different 3E states [24] -[25]. The intersystem crossing rates of $T_{1X,Y}$ exceed the rate of the ISC rate of T_{1Z} to 1A_1 by three orders of magnitude [4]. In contrast, the ISC transition rates from the singlet 1A_1 to triplet ground ground state 3A_2 k_{ST} is approximately isotropic [4]. A diagram highlighting the various optical transitions are shown in Fig. 1.5.

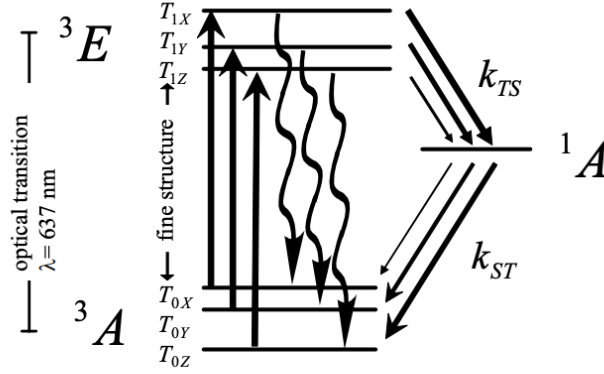


Figure 1.5: The energy level diagram of an N-V centre as well as the allowed optical transitions. The thickness of the diagonal arrows indicates the strength of spin-selective intersystem crossing transition.

As a consequence of the spin-dependent ISC transitions, it is apparent the state T_{1Z} rarely passes through the singlet state and thus the singlet state $m_S = 0$ contributes the most to the fluorescence of the NV centre [24]. Furthermore, a strong spin polarisation (> 80%) can be established after a few optical excitation and relaxation cycles among the $T_{0X,Y}$ and T_{0Z} states [4]. This spin-selective shelving into metastable singlet state forms the basis of optical readout[4]. The next chapter discusses this topic in more detail.

1.2.2 Photoluminescence spectrum

Strong electron-phonon coupling of the excited states, give rise to vibrational transitions between two electronic states, whereby phonon⁴ are absorbed by electrons upon optical excitation, thereby gaining more energy and emitting higher energy photons after relaxation, resulting in a phonon emission band called the phonon sideband [7]. After excitation the electron is promoted to one of the highly excited vibrational levels of the excited state 3E

⁴quanta of energy due to the vibration of the diamond crystal

, thereafter undergoing a fast internal conversion to the zero-phonon level⁵ [24]. From here the electron can either emit an electron or pass through the singlet state 1A_1 [24]. This scheme is illustrated in Fig. 23 [24].

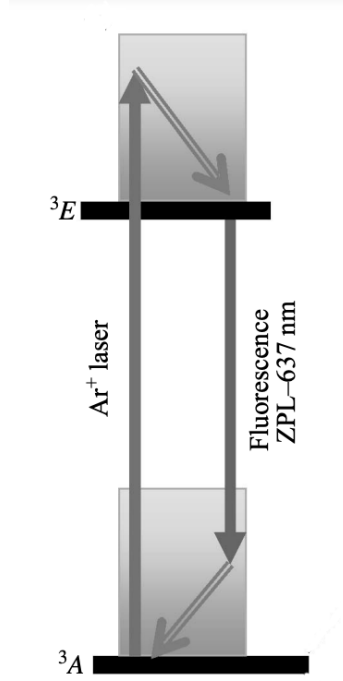


Figure 1.6: The average decay pathway of an NV centre after being excited by an Ar⁺ laser ($\lambda = 514.5$ nm).

Thus, from the contributions of the phonon-assisted emissions, the spectral spectrum of the NV centre is expected to contain a characteristic sharp peak connected a zero-phonon transition as well as other peaks that make up the phonon sideband. Experiments show the NV centre has a broad photoluminescence spectrum and the zero phonon line(ZPL) contributes only 4% to the overall intensity after optical excitation[21]. The photoluminescence spectrum of the NV centre is depicted in Fig. 1.7[6].

⁵the energy level the electron would be promoted to in the absence of phonon coupling

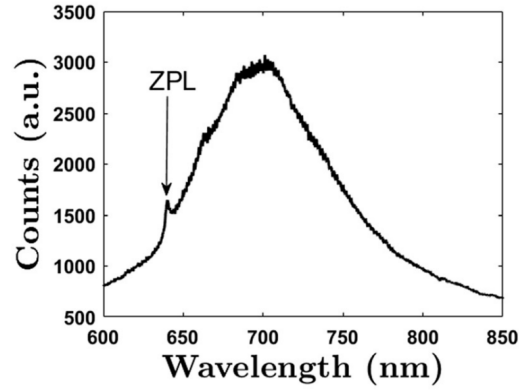


Figure 1.7: The emission spectrum of the NV centre is made up of the zero phonon line which depicts a purely radiative transition at 637 nm and phononic sidebands which extend to approx. 800 nm.

When the NV centre passes the singlet state 1A_1 it does not fluoresce in the 600 - 850 nm band, however, decaying directly to the ground state 3A_2 produces fluorescence in the 600 - 850 nm band. Since radiative transitions are spin-selective, the $m_S = \pm 1$ states therefore contribute less to this PL band on average. The contrast in fluorescence is shown Fig. 1.8 [26].

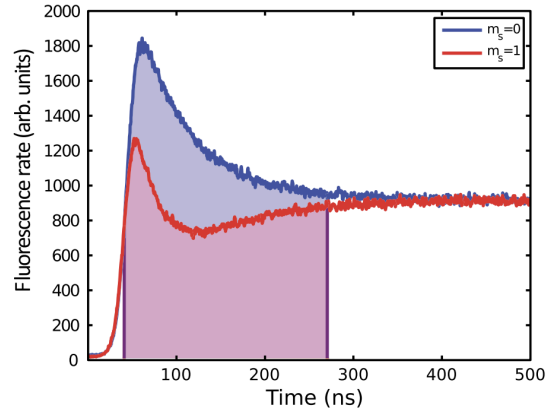


Figure 1.8: The state-dependent fluorescence measurement from the NV centre spins. The $m_S = 0$ state emit photons at greater rate than $m_S = \pm 1$ spin states.

Spin-dependent fluorescence profiles are useful for optical readout protocols to determine the state of the NV centre [26].

To obtain a narrower PL spectrum, it's natural to cool the NV centre to reduce the phonon interactions, however, at low temperatures, the detection of NV centres had proven to be more difficult as the the average fluorescence intensity emitted by the centre

dropped[24]. This is due to the absence of the dominant phonon induced transition between 1A and 3E which depopulates the singlet state 1A . Thus, upon optical excitations of $\lambda = 547\text{nm}$ light, the excited electrons become trapped in the singlet state and remain there for a long time [24]. However, at room temperature the phonon-induced transition $^1A \rightarrow ^3E$ effectively depopulates the singlet state 1A and we can obtain a reliable average fluorescence intensity for the centre[17]. Only recently, the problem of the experimental observation of single NV centres at low temperatures was solved, which made it possible to measure the correlation function $g^2(\tau)$ of the fluorescence intensity emitted by centres [24]-[27]. The second correlation function $g^2(\tau)$ is discussed in detail next.

1.2.3 NV centre as single photon source

The NV centre is often approximated as a 2-level system and is prominent candidate for application as a single photon source for its room temperature high radiative quantum efficiency as well as its short radiative lifetime [28]. A single-photon source is a device that should emit exactly one photon upon excitation by a trigger pulse, either electrical or optical [29]. A single photon source includes an emissive structure such as an atom and a trigger pulse (typically a laser) to excite the structure to an excited state, whereby a cascade of photons are emitted during relaxation to the ground state, as shown in Fig. 14 [29].

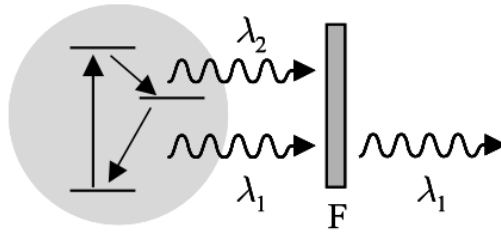


Figure 1.9: An emissive species emits photons of different wavelengths as it decays, however, a selective filter ensures only one of the photons is collected.

The emissive structure usually emits photons with different frequencies, however, it is possible to collect only one of the photons from the initiated transition by filtering the fluorescence with a selective filter [29]. This ensures that when an intense optical pulse triggers rapid excitations, the species will only emit one photon at a time, approximately equal to the radiative lifetime τ_R of the species [29]. This creates time gaps between the emitted photons and so non-classical light called antibunched light is produced [29]-[30].

Light can be characterized according to the second order correlation function $g^2(\tau)$,

or more precisely, the types of light differ by the value of $g^2(\tau)$ when $\tau \sim 0$ [29]. The classification of light proceeds as follows:

- Bunched light: $g^2(0) > 1$
- Coherent light: $g^2(0) = 1$
- Antibunched light: $g^2(0) < 1$

A simplistic illustration of the differences is shown in Fig. 1.10 [29].

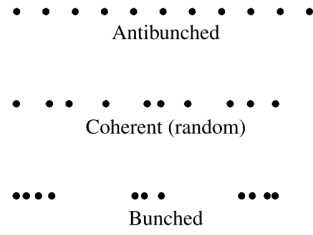


Figure 1.10: Photon beam comparisons for the different types of light. The three lights vary by their photon statistics. There are limits to the capabilities of emitting structures such as the NV centre, as the process of spontaneous emission is probabilistic, photons will not be emitted at the same time for each excitation-emission cycle, thus the depiction is the idealised version of antibunched light but it cannot be produced in practice.

The second correlation function $g^2(\tau)$ is measured through photon counting events based on the Hanbury Brown–Twiss (HBT) experiment [29]. The experimental setup for a typical g^2 measurement is shown in Fig. 1.11 [29] and described below.

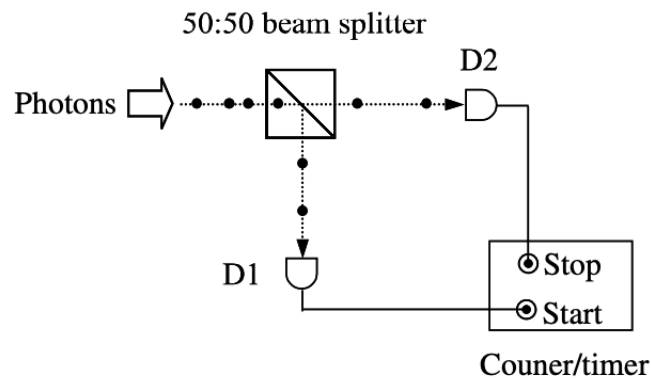


Figure 1.11: Simplified HBT configuration whereby the emitted photons are incident on a beam splitter.

A stream of photons are channeled on a 50 : 50 beam splitter, where the beam is divided

equally, with two beams exiting output ports. The photons impinge on detectors(D1 or D2), generating output pulses that are supplied into an electronic timer. The counter/timer measures the time between pulses from D1 and D2, and counts the number of pulses at each input. The results of the experiment are generally presented in a histogram, as shown in Fig. 1.12 [28].

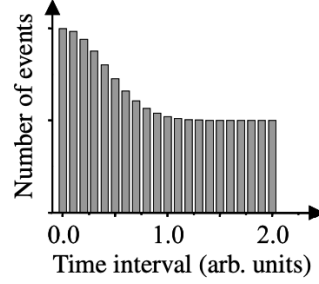


Figure 1.12: The histogram charts the number of events that are captured for each period of time τ between the start and stop pulses. This histogram displays the results of bunched light, there are more correlated detections for small intervals τ meaning the photons reaches both detectors at roughly the same time.

The histogram shows the number of events detected for each time interval, τ between the start and stop pulses [29]. Photons strike the beam splitter one at a time, being randomly directed to detectors D1 or D2 with equal probability. This gives a 50% chance that a photon will be detected by D1, triggering the timer to start recording. If D1 registers a start pulse, there is a zero percent chance of getting a stop pulse from D2 for that photon, so no events are recorded at $\tau = 0$. Therefore, no events are expected at $\tau = 0$, but events are more likely to occur at larger values of τ . The non-classical result, where $g^2(0) = 0$, arises because the photon stream consists of individual photons with long intervals between them [28]. Now, consider a scenario where photons arrive in groups. Half of the photons are directed to D1 and the other half to D2. When these photon groups hit the detectors simultaneously, there is a high probability that both detectors will register at the same time, resulting in many events near $\tau = 0$. As τ increases, the likelihood of a stop pulse after a start pulse decreases, leading to fewer recorded events. Thus, many events occur near $\tau = 0$, with fewer at later times. Therefore, g^2 represents the conditional probability of detecting a second photon at time $t = \tau$, given one was detected at $t = 0$. This is exactly what the HBT experiment's histogram with photon-counting detectors shows, providing a direct measurement of the second-order correlation function $g^2(\tau)$ [28].

Before performing a g^2 measurement it's important that the emissive species must be isolated and its fluorescence rate must be regulated [29], thus the NV centre fluorescence must be extracted properly. An isolated NV centre is optically triggered from the ground

to the excited level by light of wavelength of 532 nm [28]. To focus on a single point defect, the diamond sample can be carefully positioned in three dimensions using a variable translation stage [28]. The pump light was focused onto the NV centre using a relay lens and microscope objective lens to spot of 430 nm inside the diamond. The emitted fluorescence light is coupled via a confocal microscope arrangement into a single-mode optical fiber as shown in Fig. 1.13 [28].

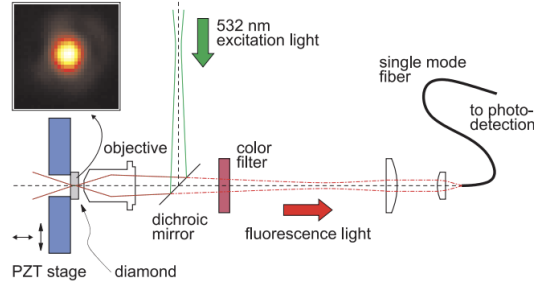


Figure 1.13: Experimental setup to collect single-photon fluorescence from an NV centre.

A dichroic mirror and a colour glass filter is used to prevent pump light coupling in the fluorescence detection system [28]. The detected light has a broad fluorescence emission in the red region, with Raman scattering contributions between 570 and 620 nm. In the HBT configuration, Raman-scattered light is blocked with a red-colored glass filter to preserve single-photon statistics attributed to the transitions [28]. Fluorescence light is sent through a beam splitter and two filters RF(to block Raman-scattered light), SF(to prevent crosstalk) onto two photodiodes D1, D2, to record the detection time difference $\tau = t_2 - t_1$ [28].

The number of data points captured in each time bin is divided by $r_1 \times r_2 \times t_{bin} \times T_{int}$, to calculate the experimental correlation function $g_m^2(\tau)$ where r_1 and r_2 are the mean count rates per second, t_{bin} the time bin width, and T_{int} the total integration time [28]. Antibunching was observed around $\tau \sim 0$ as seen in Fig. 1.14, where the minimum value $g_m^2(\tau = 0) = 0.26$ was obtained for a pump power of 5 mW, the experimental results are show the NV centre has a strong antibunching signature [28]. With increasing τ , the antibunching signature in $g_m^2(\tau)$ decays exponentially [28].

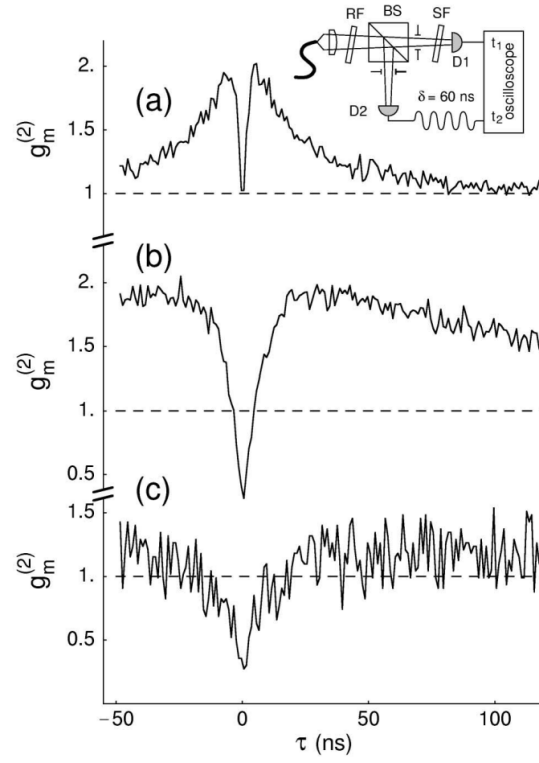


Figure 1.14: Antibunching experiment histogram plot for different pump laser light excitation powers.)

For applications, where a high yield in the narrow wavelength bands is essential, optical cavities can be employed. Specifically, the cavity can preferentially enhance the emission at the wavelength corresponding to its resonant mode, leading to a higher emission rate (Purcell enhancement) for that particular wavelength (ZPL) $\lambda = 637$ nm [28],[31]-[32].

Chapter 2

Quantum Computing Operations

2.1 Linear Optical Quantum Computing

2.1.1 Single photons as qubits

Unlike many quantum mechanical systems, single photons are particularly robust to noise or decoherence and can be manipulated easily to form one-qubit logic gates and allow information to be encoded using many different degrees of freedom such as polarisation and path [1]. Photons exhibit polarisation, and schemes have utilized this two-level degree of freedom photons possess when encoding qubits [1].

A single qubit can be represented using two orthogonal polarisation states for a single photon such as $|H\rangle$ and $|V\rangle$ as the basis, therefore an arbitrary qubit has the form $\alpha |H\rangle + \beta |V\rangle$ where $|\alpha|^2 + |\beta|^2 = 1$ [1]. The states can be plotted on a Poincaré sphere shown in Fig. 2.1 and are known as the planes of vibration of the transverse electric field in light, $|H\rangle$ and $|V\rangle$ refer to horizontally and vertically polarised light, respectively [1].

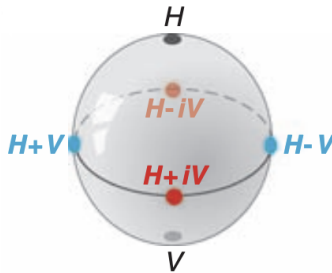


Figure 2.1: The polarisation state of single photon can be given in Bloch representation using this Poincaré sphere

Single qubit gates can be realized by implementing half and quarter wave plates¹ that rotate the polarisation states on the sphere, by either a half-rotation or a quarter-rotation respectively [1]. A $1/4 - 1/2 - 1/4$ wave plate configuration performs an arbitrary rotation on the initial $|H\rangle$ photon with the output state being a superposition of the basis ($|H\rangle, |V\rangle$) [1]. The transformation is illustrated in Fig. 2.2.

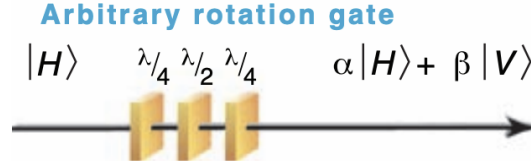


Figure 2.2: An arbitrary rotation of a single photons polarisation state achieved by a $1/4 - 1/2 - 1/4$ sequence

In the single qubit gate scheme the single photon encounters a polarising beam splitter(PBS) which transmits $|H\rangle$ and reflects $|V\rangle$, this effectively converts the polarisation encoding to path encoding, specifically $|H\rangle \rightarrow |0\rangle$ where $|0\rangle$ represents the upper path and $|V\rangle \rightarrow |1\rangle$ where $|1\rangle$ represents the lower path [1]. The single qubit operation is shown in Fig. 2.3.

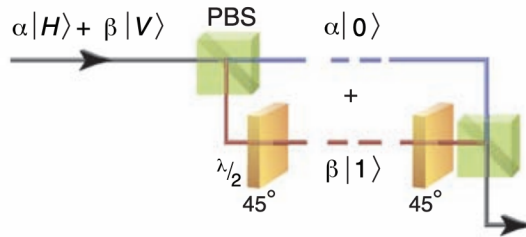


Figure 2.3: Converting between polarisation and path encoding is realized using a PBS, allowing transmission of $|H\rangle$ and reflecting $|V\rangle$ as well as using half-wave plate oriented at 45° induces $|V\rangle \leftrightarrow |H\rangle$ rotations.

2.1.2 Linear Optical Network

While creating single qubit gates for optical quantum computing is fairly trivial, realizing entangling logic gates is a more challenging and vital task for quantum computation [1]. The prime example of such a gate is the controlled NOT(CNOT) gate which works by flipping the state of a target qubit when the control qubit is in the state “1”, however this flip is conditional as when the control qubit is in state “0”, no flip on the target

¹Wave plates utilize the optical property of birefringence to rotate polarisation states

qubit is executed [1]. Following the single qubit encoding - this qubit would be the target qubit - the two paths are combined at a 50:50 beam splitter (shown in Fig. 2.3) which mixes the path states into a coherent superposition $|0\rangle + |1\rangle / \sqrt{2}$ [1]. A CNOT gate would apply a π phase shift where $|0\rangle + |1\rangle / \sqrt{2} \rightarrow |0\rangle - |1\rangle / \sqrt{2}$ if the control qubit is in “1” [1]. A scheme to implement this conditional phase shift is shown in Fig. 2.4 [1]. The scheme goes as follows: the polarisation encoded control and target qubits along with two supplementary photons, enter an optical platform consisting of four beam splitters, and the four photons’ paths are combined [1]. Exiting the optical network, if a single photon is detected at each detector, a CNOT operation is applied to the control and target qubit, however if any other detection event occurs a CNOT operation isn’t applied [1]. Therefore, the CNOT gate is probabilistic which is not very useful for quantum computing as for many CNOTs the probability that the computation succeeds is very low [1]. However, by using more photons, a near deterministic CNOT can be realised [1]. Schemes utilizing more than 10,000 pairs of photons achieved a success probability greater than 95%, however this places a large resource overhead making optical quantum computing impractical [1]. Optical quantum computing is still sought after today as there have been new proposals that reduce the resource overhead such as cluster state computing which utilizes the probabilistic nature of the CNOT gates, this as well as other approaches have seen promising but no demonstrations using an NV centre as a single photon source has received notable attention [1].

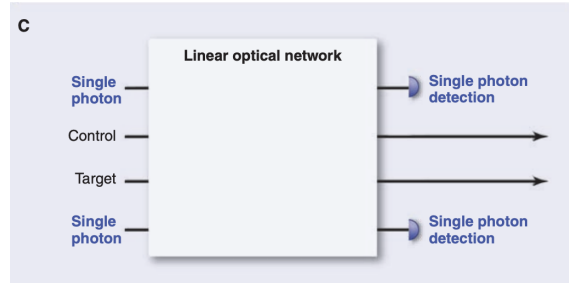


Figure 2.4: Schematic diagram of the nondeterministic CNOT gate

While impurities in diamond are well suited as optical centres for single photon generation, the NV centre falls behind other defects such as the silicon-vacancy (SiV) centre and nickel-nitrogen complex (NE8) due to its lack of inversion symmetry, broad emission bandwidth, weak ZPL emissions and relatively long decay time leading to a lower single photon generation rate [32]. Therefore, the NV centre is not an ideal single photon source, however, their electron-nuclear qubits could be utilized to store information in hybrid approaches [1]. Their spin qubits are discussed in the next section.

2.2 NMR Quantum Computing

2.2.1 Initialization and Optical Readout

As mentioned in section 2.2, the spin dependent fluorescence of the NV centre can be explained by the different dominant relaxation mechanisms of the spin projections from the excited state 3E to ground state 3A_2 [7]. The preferential decay pathways are highlighted again in Fig. 2.5 [7].

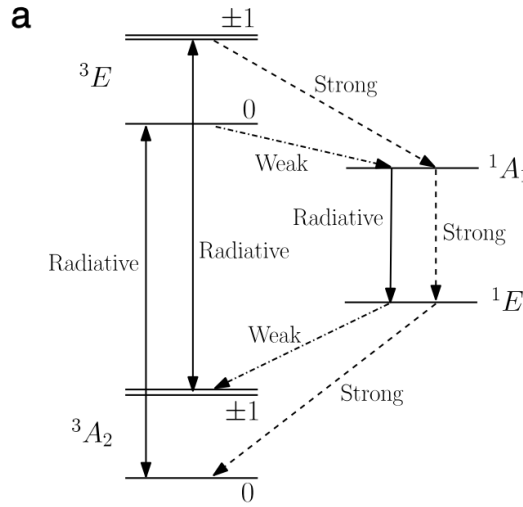


Figure 2.5: Illustration of the strong and weak decay pathways along the NV centre energy levels.

The ISC rate from the excited state to the singlet 1A by non-radiative decay is much greater for the $m_S = \pm 1$ than for the $m_S = 0$ spin projection, and the ISC rate of the singlet state to the ground state are approximately equal. The 1A singlet state has higher probability to relax to the $m_S = 0$ ground state sublevel than to the $m_S = \pm 1$ sublevel, this results in a resultant polarization into the ground $m_S = 0$ state [12]. Therefore, after a few cycles of off-resonant (to excite all ground spin sublevels) excitation pulses, the probability to find the NV centre in the $m_S = 0$ sublevel of the ground state is much higher than for the $m_S = \pm 1$ sublevel, this process is known as optical spin-polarisation. The electron spin of the NV centre can be initialized into the $m_S = 0$ spin projection to an electron spin polarisation of 0.83 [27].

NV centres in diamond appear as bright red spots when illuminated by laser light. The NV centres in the state $|0\rangle$ fluoresces more intensely than centres in the $|\pm 1\rangle$, as shown in Fig. 23. $|0\rangle$ is commonly referred to as the bright state and $|\pm 1\rangle$ are called the dark states [5].

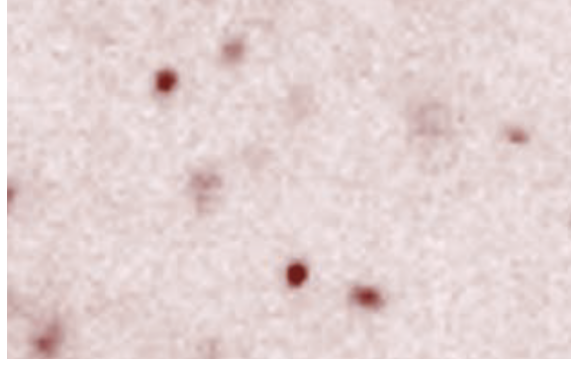


Figure 2.6: Red light emission from single NV spin transitions occurring within diamond sample

As seen, the optical dynamics of the NV centre allow for the the polarisation of the NV centre spin into the $m_S = 0$ spin orientation and optical readout of the centre's spin state [7]. Optical readout is conducted through measurement of the fluorescence intensity, which indicates the state of the NV centre's spin sublevel, this technique is known as Optically Detected Magnetic Resonance(ODMR)² [6]-[12]

2.2.2 NV centre electronic spin control

The NV electron spin has a triplet ground state comprised of a highly emissive state $|0\rangle$ and two degenerate states $|\pm 1\rangle$ with a zero-field splitting of $D = 2.87$ GHz [31]. Applying an external field to the NV centre, induces Zeeman splitting and lifts the degeneracy of the two sublevels $|1\rangle$ and $|-1\rangle$ [7]. Applying a strong microwave field in resonance with the $|0\rangle \rightarrow |1\rangle$ transition frequency with approximate form $b_1 \cos \omega t$ induces Rabi oscillations as seen in Fig. 2.7 [31]. The spin state flips back and forth between the two spin state with frequency $\omega_{NV} = \gamma_{NV} b_1$, whereby γ_{NV} is the gyromagnetic ratio of the NV electron spin and thus the oscillation frequency is dependent on the magnitude of b_1 [31].

²In an ODMR scan, a sample is illuminated with band of pulse frequencies and the corresponding fluorescence is measured, the fluorescence profile at certain frequencies reveals the resonances and transitions occurring within the sample

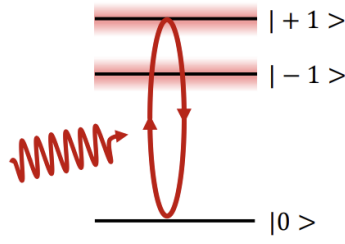


Figure 2.7: The simplified energy levels of the NV centre. A resonant microwave pulse drives the oscillation between the spin sublevels $|0\rangle$ and $|1\rangle$.

If the NV centre is treated as two level system of $|0\rangle$ and $|1\rangle$, the superposition of the two states can approximate a qubit by definition. The NV centre is initialised in the ground state spin sublevel by green laser light illumination [6]. Following this, a microwave(mw) pulse with frequency ω_{NV} is applied which rotates the NV centre spin sublevels resulting to an oscillation in population between the $|0\rangle$ and $|1\rangle$ spin states [6]. This is called Rabi flopping and is show in Fig. 2.8 accompanied with a Bloch sphere representation of the Rabi oscillations [6]. The Bloch sphere is modeled with the Bloch vector (red arrow) which represents the instantaneous spin state of the system during evolution and \hat{x} and \hat{y} indicate the polarization of the driving field in the rotating frame [6]. The Bloch vector rotates at a speed depending on the magnitude of the mw field around an axis dependent on its phase (blue curve) [6]. A 180 degree rotation around the sphere corresponds to the mw field transferring the population from $|0\rangle$ to $|1\rangle$, is referred to as a π -pulse [6]. Consequently a $\frac{\pi}{2}$ -pulses leads to a 90 degree rotation of the state-vector from the $|0\rangle$ axis, creating a superposition state between $|0\rangle$ and $|1\rangle$, $\frac{|0\rangle+|1\rangle}{\sqrt{2}}$ which lies on an axis perpendicular to the axis representing $|0\rangle$ and $|1\rangle$ [6].

The microwave field induced nutations approximate the realisation of a coherent NOT gate, a crucial logic gate for quantum computation[8].

2.2.3 Hyperfine Interactions

The nuclear spin of ^{13}C has been identified as compatible to devise a two-qubit system, this system allows for high-fidelity polarization and detection of single electron and nuclear spin states, even under ambient conditions [23].

The carbon-12 isotope with nuclear spin $I = 0$ is the most abundant in the diamond sample, whereas the natural concentration of carbon-13 isotope possessing nuclear spin $I = 1/2$ is 1.1% [25]. Thus on average there should be one ^{13}C present in the first coordination shell of the defect centre for every 30 defect centres [25]. The hyperfine coupling between the electron spins and nuclear spins is a function of spin density and therefore decreases

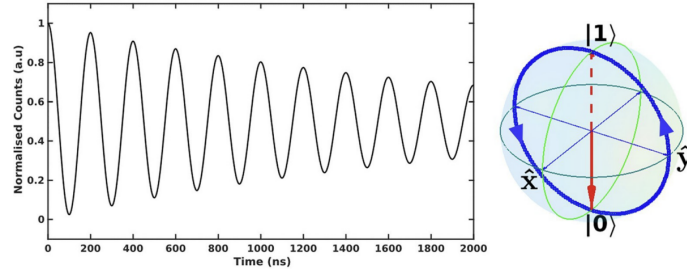


Figure 2.8: Following initialisation to $|0\rangle$ resonant mw pulses induce magnetic dipole transitions altering the ground-state spin polarization which leads a reduction of the fluorescence intensity. The diagram on the left indicates the oscillations in the fluorescence intensity and the diagram on the right is the Bloch sphere representation for the transitions. The apparent decay of the amplitude of oscillation is caused decoherence induced by continuous spin measurements.

exponentially with distance from the vacancy according to the McConnell relation [25]. Consequently, the hyperfine coupling constants between proximal and distant spins differ by tens of MHz [25]. In the presence of a static magnetic applied along the axis($\langle 111 \rangle$ crystallographic axis) the $I = 1/2$ nuclear spin experiences nuclear Zeeman splitting and the degeneracy between the $m_I = 1/2$ and $m_I = -1/2$ nuclear spin is removed [30]. The transition frequency between the two spin sublevels $m_I = 1/2$ and $m_I = -1/2$, however, is not the same for all nuclear spins in the lattice, this non equivalence is caused by the hyperfine interactions and is proportional to the hyperfine coupling constant addressed earlier[25]. As a result of an enhanced magnetic moment and hyperfine interactions, the single nuclear spins can be distinguished from one another and the environment, enabling the addressing of single nuclear spins [14]. An electronic spin $m_S = 0$ does not couple with nuclear spins and only the $m_S = 1$ contributes to the unique splitting ω_1 between the energy levels [25]. Thus certain nuclear spins can be controlled using the coupling and rf pulses [5]. Nuclear spins with a particular transition frequencies can be driven by a rf pulse, causing spin flips for only a select few proximal nuclear spins [14]. Additionally, the spin flip is conditional on the state of the electron spin, as when the electron spin is $|0\rangle$ the π -pulse doesn't result in a spin flip [5]. This conditional coupling of the nuclear spin to the electronic spin forms the basis for the implementation of quantum logic gates such as CNOT gate [5].

2.2.4 Hyperfine Structure

The hyperfine interactions between the defect spin and a ^{13}C atom that replaces one the ^{12}C splits the fine structure even in the absence of an external magnetic. The additional splittings appear in the electron paramagnetic resonance(ESR) spectra shown in Fig. 2.9 [25].

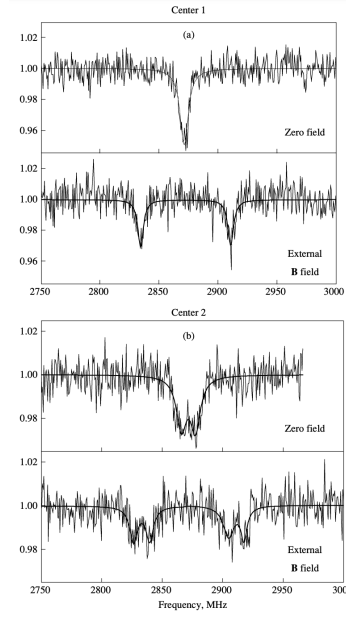


Figure 2.9: Optically detected ESR spectra of single NV centre, showing sharp changes in fluorescence after resonant transitions. In a) There is no external magnetic field and no hyperfine interactions(upper) and there is an external magnetic field but no hyperfine interactions(lower) b) Spectrum shows hyperfine for no magnetic field(upper) and when a magnetic field is applied(lower)

The NV centre electronic spins $m_S = 0$, $m_S = \pm 1$ couple with the single carbon-13 atom spins $m_I = -1/2$ and $m_I = 1/2$ through hyperfine interactions resulting in the hyperfine split electron spin sublevels of the form $|m_S, m_I\rangle$ with four possible configurations [23]. The hyperfine structure of the $\text{NV} + ^{13}\text{C}$ defect centre is shown in Fig. 2.10 [25].

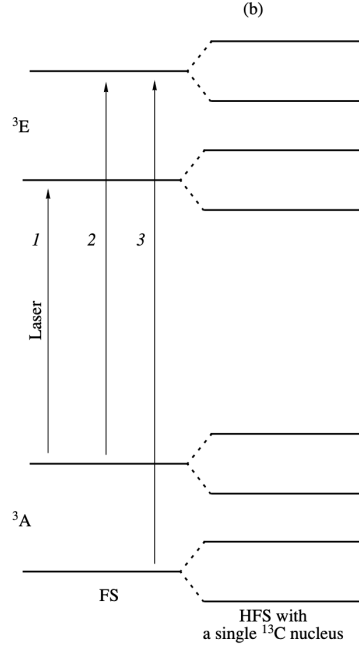


Figure 2.10: The simplified energy level diagram of the hyperfine structure of the $NV + {}^{13}C$ defect system

2.2.5 Two-Qubit Operations

In this section a scheme for the realization of electron-nuclear two-qubit gate is explored [16]. Employed radio-frequency (RF) control as well as dynamical decoupling (DD) of the electron spin [16]. The objective of the scheme is to control proximal nuclear spin and optimise the coherence of electron spin. The $NV + {}^{13}C$ system Hamiltonian is given by:

$$H = \omega_L I_z + A_{\parallel} S_z I_z + A_{\perp} S_z I_x \quad (2.2.1)$$

where $\omega_L = \gamma B_z$ is Larmor frequency determined by the magnitude of the external magnetic field along the $\langle 111 \rangle$ crystalline direction, γ is the gyromagnetic ratio for the ${}^{13}C$ spin, S_{α} is the $S=1$ spin projector for the electron spin and I_{α} is the $I=1/2$ nuclear spin projector, A_{\parallel} and A_{\perp} are the parallel and perpendicular hyperfine components, respectively [16]. Radiofrequency pulses of Rabi frequency Ω , phase ϕ and frequency ω are applied to the nuclear spin for coherent control. The frequency ω is set to the spin precession frequency ω_1 of the nuclear spin under the influence of the electron spin $m_S = 0$, thus the RF pulse targets particular nuclear spins. It is assumed that $(\omega_L - \omega_1) \gg \Omega$ and the perpendicular hyperfine component is neglected for simplicity [16].

By only considering the spin sublevels $|0\rangle$ and $|-1\rangle$ for the subspace and applying a driving RF pulse, the Hamiltonian transforms to in the rotating reference frame of the RF

frequency:

$$H = |0\rangle\langle 0| \otimes (\omega_L - \omega_1)I_z + \quad (2.2.2)$$

$$|1\rangle\langle 1| \otimes \Omega(\cos(\phi)I_x + \sin(\phi)I_y) \quad (2.2.3)$$

where here $|1\rangle$ represents the $m_S = -1$ spin projection. Consequently, the electron spin being in the state $|0\rangle$ leads to the nuclear spin processing around the \hat{z} axis at frequency $(\omega_L - \omega_1) = A_{||}$. Alternatively, the electron spin being in the state $|1\rangle$ leads to nuclear spin processing around a rotation axis in the xy -plane determined by the RF field phase ϕ [16]. While at the same time the nuclear spin is coupled with the electron spin, an RF field with the sequence $(\tau - \pi - 2\tau - \pi - \tau)^{N/2}$ to decouple the electron spin as we apply the RF pulses. The total number of decoupling pulses is given by N and the π denotes a π -pulse to the electron spin and τ is the time interval between the π -pulses. The nuclear spin evolution during this sequence depends on the initial state of the electron spin [16].

Each RF pulse applied to rotate the nuclear spin during the sequence is assigned an integer starting with 1 and ending with K , whereby K is the sum of the RF pulses applied in the sequence given by $K = N + 1$. If the initial spin state of the electron is $|0\rangle$, the first RF pulse will not drive the nuclear spin, only once the electron spin state is flipped to $|1\rangle$ will the RF pulse rotate the nuclear spin. Thus, for an initial state $|0\rangle$, only the even k RF pulses are resonant and consequently for the initial electron spin projection $|0\rangle$, only the odd k RF pulses are resonant [16]. This scheme is illustrated in Fig. 2.11 [16].

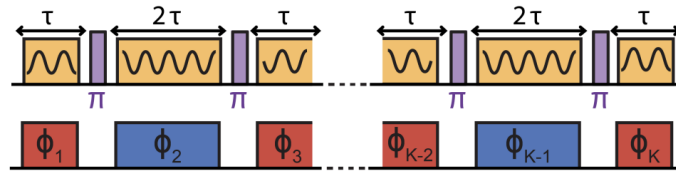


Figure 2.11: The dynamic decoupling and radiofrequency sequence DDRF used to construct a quantum logic gate using the $NV + ^{13}C$ defect system. The representations are: RF pulses as yellow, dynamic decoupling pulses as purple, resonant RF pulse for the initial state $|1\rangle$ is red and resonant RF pulse for the initial state $|0\rangle$ is blue.

An unconditional and conditional rotation corresponding to a single qubit and two qubit gate respectively are modeled by calibrating the phases ϕ_k of the RF pulses [16]. The required phases for the RF pulses so that they build up constructively are given by

$$\phi'_k = \begin{cases} (k-1)\phi_\tau + \pi & k \text{ odd} \\ (k-1)\phi_\tau & k \text{ even} \end{cases} \quad (2.2.4)$$

The additional phase π shift to the odd k sequence converts the unconditional rotation to a conditional rotation [16]. Further addition of the phase ρ to all RF fields, the gate rotation

axis is established, the RF pulse phase are thus given by $\phi_k = \rho + \phi'_k$ [16]. Subsequently, the evolution of the two-qubit system is described by $V = V_z \cdot V_{CROT}$, where V_z corresponds to the unconditional precession of the nuclear spin around the z axis and V_{CROT} corresponds to the electron state dependent rotation of the nuclear spin [16]. V_{CROT} is given by

$$V_{CROT} = |0\rangle\langle 0| \otimes R_\rho(N\Omega\tau) + \quad (2.2.5)$$

$$|1\rangle\langle 1| \otimes R_\rho(-N\Omega\tau) \quad (2.2.6)$$

where $R_\rho = e^{-i\theta(\cos(\rho)I_x + \sin(\rho)I_y)/\hbar}$. Moreover, this depicts the controlled rotation of the nuclear spin to an angle (set by N , Ω and τ) and rotation axis (given by ρ). For $N\Omega\tau = \pi/2$, the gate operation leads to a $\pi/2$ rotation on the nuclear spin when the electron spin is $|0\rangle$ and a $-\pi/2$ inversion when the electron is in state $|1\rangle$. The gate operation for a $N=8$ pulse sequence is illustrated in Fig. 2.12 with a Bloch sphere [16]. The $N\Omega\tau = \pi/2$ gate executes a maximum entanglement two-qubit operation, equivalent to a controlled-not (CNOT) gate up to local rotations [16]. To execute a two-qubit operation, the prepare the electron spin must first be prepared in a superposition state before executing the DDRF controlled-rotation, after the rotation the electron and nuclear spins are said to be then maximally entangled with form:

$$|\Psi_{Bell}\rangle = \frac{|0, \downarrow\rangle + |1, \uparrow\rangle}{\sqrt{2}}$$

where the up and down arrow kets correspond to the spin-up and spin-down nuclear spin projections [16].

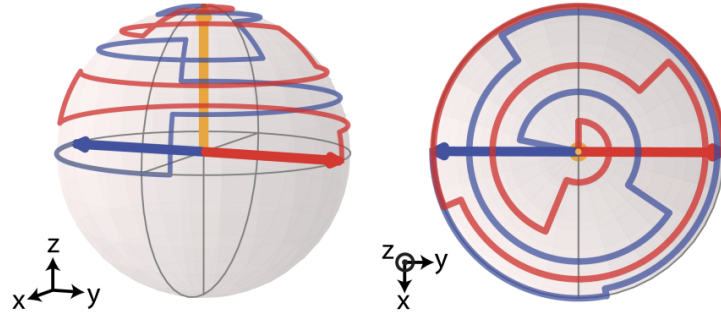


Figure 2.12: Bloch sphere representation of the evolution of the initial nuclear spin (yellow), the $\pi/2$ ($-\pi/2$) rotation is marked in blue (red) when the electron spin state was $|0\rangle$ ($|1\rangle$). The diagram on the left gives the side view and the right gives the top-down view of the nuclear spin evolution on the Bloch sphere. If the initial state of spin nuclear spin points in one direction, say $|\uparrow\rangle$, then depending on whether the electron spin is $|0\rangle$ or $|1\rangle$, the nuclear spin will rotate to either $|\leftarrow\rangle$ (blue) or $|\rightarrow\rangle$ (red), respectively.

The techniques have been applied to realize a 10-qubit hybrid spin register involving

one central electron spin, one 14^N spin and eight ^{13}C spins, where two-qubit gates using the DDRF scheme are utilized for preparation of an electron-nuclear Bell state and nuclear-nuclear entanglement is achieved through different schemes [16]. These two-qubit entangled state can be stored for over 10 seconds and single qubit gates can be stored for up to 63 seconds, meaning long-lived quantum memory can be effectively implemented into the 10-qubit register[16].

2.3 Conclusions

In this essay we examined how the NV diamond can be used as a platform for the physical realization of QIP. The NV centre has an elaborate energy structure as well as well defined quantum states within the band-gap that can be easily initialized through optical pumping and read out by observing the fluorescence intensity. Additionally, spin states are controlled using magnetic resonance techniques, while the rigid diamond lattice provides protection from thermal decoherence, allowing for relatively long coherence times, even at room temperature. These simple processes of initializing, manipulating, and reading quantum states make the NV system a promising platform for quantum information processing (QIP), even at room temperature. Furthermore, hyperfine coupling between electronic spins and nuclear spins gave rise to a hyperfine structure and schemes to control nuclear spins. Additionally, it was concluded that other defect centres are more suitable than the single NV centre in diamond as a single photon source.

In conclusion, we have developed a novel two-qubit gate for electron- nuclear systems and discussed how it can be applied to realize a long-lived 10-qubit solid-state spin register. The techniques in this work can be applied to multi-qubit control in other defect platforms as well. From these methods as well as more schemes emerging from QIP research, it seems possible that quantum computers featuring multiple qubits using an NV centre quantum register platform could become implemented.

The spin-dependent PL spectrum observed implies the presence of dark states and provides the basis of optical readout, and the spin-selective decay pathways to the dark ways is necessary for spin polarisation. The employment of NMR techniques from the single qubit operations as well the exploitation as the magnetic dipolar coupling was exploited were combined to establish long-living electron-nuclear spin entanglement. An electron-nuclear two-qubit system was used for the implementation of a conditional two-qubit gate V_{CROT} . This gate applies a rotation of the nuclear spin depending on the orientation of the electron spin. With the quantum logic gates system demonstrated, the realization of a quantum processor with 12 or more quantum bits seems to be achievable, possibly not with the NV centre defect and a optically active solid state structure.

Section 2.2 discussed how the NV centre ground state can be treated as a two-level spin

system by initialising the system in the $m_S = 0$ state and applying microwave excitaitons to the $m_S = -1$ state, the ground state that can be used as computational basis for QIP where $m_S = 0 \rightarrow |0\rangle$ and $m_S = -1 \rightarrow |1\rangle$. The Hyperfine Coupling is also essential to create controlled gates with the two qubits, as it governs the interaction between them. Under techniques applying radiofrequency pulse sequences, a quantum logic gate CROT can be realised. Quantum protocols can be formulated to make use of the two qubits in QIP.

Bibliography

- [1] J. L. O’Brien, *Optical quantum computing*, *Science* **318** (2007), no. 5856 1567–1570.
- [2] P. Neumann, R. Kolesov, B. Naydenov, J. Beck, F. Rempp, M. Steiner, V. Jacques, G. Balasubramanian, M. Markham, D. Twitchen, et al., *Quantum register based on coupled electron spins in a room-temperature solid*, *Nature Physics* **6** (2010), no. 4 249–253.
- [3] A. Tsukanov, *Nv-centers in diamond. part i. general information, fabrication technology, and the structure of the spectrum*, *Russian Microelectronics* **41** (2012) 91–106.
- [4] F. Jelezko and J. Wrachtrup, *Quantum information processing in diamond*, *arXiv preprint quant-ph/0510152* (2005).
- [5] D. D. Awschalom, R. Epstein, and R. Hanson, *The diamond age of spintronics*, *Scientific American* **297** (2007), no. 4 84–91.
- [6] P. Rembold, N. Oshnik, M. M. Müller, S. Montangero, T. Calarco, and E. Neu, *Introduction to quantum optimal control for quantum sensing with nitrogen-vacancy centers in diamond*, *AVS Quantum Science* **2** (2020), no. 2.
- [7] M. W. Doherty, N. B. Manson, P. Delaney, F. Jelezko, J. Wrachtrup, and L. C. Hollenberg, *The nitrogen-vacancy colour centre in diamond*, *Physics Reports* **528** (2013), no. 1 1–45.
- [8] F. Jelezko and J. Wrachtrup, *Read-out of single spins by optical spectroscopy*, *Journal of Physics: Condensed Matter* **16** (2004), no. 30 R1089.
- [9] J. Orwa, A. Greentree, I. Aharonovich, A. Alves, J. Van Donkelaar, A. Stacey, and S. Praver, *Fabrication of single optical centres in diamond—a review*, *Journal of Luminescence* **130** (2010), no. 9 1646–1654.
- [10] R. E. Evans, *An integrated diamond nanophotonics platform for quantum optics*. PhD thesis, Harvard University, 2018.

- [11] D. D. Awschalom, R. Hanson, J. Wrachtrup, and B. B. Zhou, *Quantum technologies with optically interfaced solid-state spins*, *Nature Photonics* **12** (2018), no. 9 516–527.
- [12] G.-Q. Liu and X.-Y. Pan, *Quantum information processing with nitrogen–vacancy centers in diamond*, *Chinese Physics B* **27** (2018), no. 2 020304.
- [13] R. Hanson, V. Dobrovitski, A. Feiguin, O. Gywat, and D. Awschalom, *Coherent dynamics of a single spin interacting with an adjustable spin bath*, *Science* **320** (2008), no. 5874 352–355.
- [14] M. G. Dutt, L. Childress, L. Jiang, E. Togan, J. Maze, F. Jelezko, A. Zibrov, P. Hemmer, and M. Lukin, *Quantum register based on individual electronic and nuclear spin qubits in diamond*, *Science* **316** (2007), no. 5829 1312–1316.
- [15] A. Gali, M. Fyta, and E. Kaxiras, *Ab initio supercell calculations on nitrogen-vacancy center in diamond: Electronic structure and hyperfine tensors*, *Physical Review B—Condensed Matter and Materials Physics* **77** (2008), no. 15 155206.
- [16] C. E. Bradley, J. Randall, M. H. Abobeih, R. C. Berrevoets, M. J. Degen, M. A. Bakker, M. Markham, D. J. Twitchen, and T. H. Taminiau, *A ten-qubit solid-state spin register with quantum memory up to one minute*, *Physical Review X* **9** (2019), no. 3 031045.
- [17] J. R. Maze, A. Gali, E. Togan, Y. Chu, A. Trifonov, E. Kaxiras, and M. D. Lukin, *Properties of nitrogen-vacancy centers in diamond: the group theoretic approach*, *New Journal of Physics* **13** (2011), no. 2 025025.
- [18] M. W. Doherty, N. B. Manson, P. Delaney, and L. C. Hollenberg, *The negatively charged nitrogen-vacancy centre in diamond: the electronic solution*, *New Journal of Physics* **13** (2011), no. 2 025019.
- [19] J. Zhang, C.-Z. Wang, Z. Zhu, and V. Dobrovitski, *Vibrational modes and lattice distortion of a nitrogen-vacancy center in diamond from first-principles calculations*, *Physical Review B—Condensed Matter and Materials Physics* **84** (2011), no. 3 035211.
- [20] M. Doherty, F. Dolde, H. Fedder, F. Jelezko, J. Wrachtrup, N. Manson, and L. Hollenberg, *Theory of the ground-state spin of the nv- center in diamond*, *Physical Review B—Condensed Matter and Materials Physics* **85** (2012), no. 20 205203.
- [21] Á. Gali, *Ab initio theory of the nitrogen-vacancy center in diamond*, *Nanophotonics* **8** (2019), no. 11 1907–1943.
- [22] N. Manson, J. Harrison, and M. Sellars, *The nitrogen-vacancy center in diamond re-visited*, *arXiv preprint cond-mat/0601360* (2006).

- [23] P. Neumann, N. Mizuochi, F. Rempp, P. Hemmer, H. Watanabe, S. Yamasaki, V. Jacques, T. Gaebel, F. Jelezko, and J. Wrachtrup, *Multipartite entanglement among single spins in diamond*, *science* **320** (2008), no. 5881 1326–1329.
- [24] A. Nizovtsev, S. Y. Kilin, F. Jelezko, T. Gaebel, I. Popa, A. Gruber, and J. Wrachtrup, *A quantum computer based on nv centers in diamond: optically detected nutations of single electron and nuclear spins*, *Optics and spectroscopy* **99** (2005) 233–244.
- [25] J. Wrachtrup, S. Y. Kilin, and A. Nizovtsev, *Quantum computation using the 13 c nuclear spins near the single nv defect center in diamond*, *Optics and Spectroscopy* **91** (2001) 429–437.
- [26] J. F. Barry, J. M. Schloss, E. Bauch, M. J. Turner, C. A. Hart, L. M. Pham, and R. L. Walsworth, *Sensitivity optimization for nv-diamond magnetometry*, *Reviews of Modern Physics* **92** (2020), no. 1 015004.
- [27] X. Rong, J. Geng, F. Shi, Y. Liu, K. Xu, W. Ma, F. Kong, Z. Jiang, Y. Wu, and J. Du, *Experimental fault-tolerant universal quantum gates with solid-state spins under ambient conditions*, *Nature communications* **6** (2015), no. 1 8748.
- [28] C. Kurtsiefer, S. Mayer, P. Zarda, and H. Weinfurter, *Stable solid-state source of single photons*, *Physical review letters* **85** (2000), no. 2 290.
- [29] M. Fox, *Quantum Optics: An Introduction*. Oxford Master Series in Physics. OUP Oxford, 2006.
- [30] Y. Wu, Y. Wang, X. Qin, X. Rong, and J. Du, *A programmable two-qubit solid-state quantum processor under ambient conditions*, *npj Quantum Information* **5** (2019), no. 1 9.
- [31] Z. Wang, F. Kong, P. Zhao, Z. Huang, P. Yu, Y. Wang, F. Shi, and J. Du, *Picotesla magnetometry of microwave fields with diamond sensors*, *Science advances* **8** (2022), no. 31 eabq8158.
- [32] S. Pezzagna, D. Rogalla, D. Wildanger, J. Meijer, and A. Zaitsev, *Creation and nature of optical centres in diamond for single-photon emission—overview and critical remarks*, *New Journal of Physics* **13** (2011), no. 3 035024.